

Downwash airflow field distribution characteristics and their effect on the spray field distribution of the DJI T30 six-rotor plant protection UAV

Haiyan Zhang¹, Sheng Wen², Chunling Chen¹, Qi Liu³,
Tongyu Xu¹, Shengde Chen^{4,5}, Yubin Lan^{4,5*}

(1. College of Information and Electrical Engineering, Shenyang Agricultural University, Shenyang 110866, China;

2. College of Engineering, South China Agricultural University, Guangzhou 510642, China;

3. College of Agricultural Engineering and Food Science, Shandong University of Technology, Zibo 255022, Shandong, China;

4. College of Electronic Engineering (College of Artificial Intelligence), South China Agricultural University, Guangzhou 510642, China;

5. National Center for International Collaboration Research on Precision Agricultural Aviation Pesticides Spraying Technology, Guangzhou 510642, China)

Abstract: Spray characteristics are the fundamental factors that affect droplet transportation downward, deposition, and drift. The downwash airflow field of the Unmanned Aviation Vehicle (UAV) primarily influences droplet deposition and drift by changing the spray characteristics. This study focused mainly on the effect of the downwash airflow field of the UAV and nozzle position on the droplet spatial distribution and velocity distribution, which are two factors of spray characteristics. To study the abovementioned characteristics, computational fluid dynamics based on the lattice Boltzmann method (LBM) was used to simulate the downwash airflow field of the DJI T30 six-rotor plant protection UAV at different rotor rotational speeds (1000-1800 r/min). A particle image velocimetry system (PIV) was utilized to record the spray field with the downwash airflow field at different rotational speeds of rotors (0-1800 r/min) or different nozzle positions (0, 0.20 m, 0.35 m, and 0.50 m from the motor). The simulation and experimental results showed that the rotor downwash airflow field exhibited the ‘dispersion-shrinkage-redispersion’ development rule. In the initial dispersion stage of rotor airflow, there were obvious high-vorticity and low-vorticity regions in the rotor downwash airflow field. Moreover, the low-vorticity region was primarily concentrated below the motor, and the high-vorticity region was mainly focused in the middle area of the rotors. Additionally, the *Y*-direction airflow velocity fluctuated at 0.4-1.2 m under the rotor. When the rotor airflow developed to 3.2 m below the rotor, the *Y*-direction airflow velocity showed a slight decrease. Above 3.2 m from the rotor, the *Y*-direction airflow velocity started to drastically decrease. Therefore, it is recommended that the DJI T30 plant protection UAV should not exceed 3.2 m in flight height during field spraying operations. The rotor downwash airflow field caused the nozzle atomization angle, droplet concentration, and spray field width to decrease while increasing the vortex scale in the spray field when the rotor system was activated. Moreover, the increase in rotor rotational speed promoted the abovementioned trend. When the nozzle was installed in various radial locations below the rotor, the droplet spatial distribution and velocity distribution were completely different. When the nozzle was installed directly below the motor, the droplet spatial distribution and velocity distribution were relatively symmetrical. When the nozzle was installed at 0.20 m and 0.35 m from the motor, the droplets clearly moved toward the right under the induction of stronger rotor vortices. This resulted in a higher droplet concentration in the right-half spray field. However, the droplet moved toward the left when the nozzle was installed in the rotor tip. For four nozzle positions, when the nozzle was installed at 0 or 0.20 m from the motor, the droplet average velocity was much higher. However, the droplet average velocity was slower when the nozzle was installed in the other two positions. Therefore, it is recommended that the nozzle is installed at 0 or 0.20 m from the motor. The research results could increase the understanding of the downwash airflow field distribution characteristics of the UAV and its influence on the droplet spatial distribution and velocity distribution characteristics. Meanwhile, the research results could provide some theoretical guidance for the choice of nozzle position below the rotor.

Keywords: downwash airflow, spray field distribution, plant protection, UAV, characteristics

DOI: [10.25165/j.ijabe.20231602.8094](https://doi.org/10.25165/j.ijabe.20231602.8094)

Citation: Zhang H Y, Wen S, Chen C L, Liu Q, Xu T Y, Chen S D, et al. Downwash airflow field distribution characteristics and their effect on the spray field distribution of the DJI T30 six-rotor plant protection UAV. *Int J Agric & Biol Eng*, 2023; 16(2): 10–22.

1 Introduction

The past decade has seen a dramatic increase in the use of Unmanned Aviation Vehicles (UAVs), especially in China^[1]. Compared to piloted aircraft, UAVs are more maneuverable, do not

require a special landing airport, and can execute low-altitude spraying operations^[2,3]. Compared to ground-based plant protection machinery, UAVs are more environmentally adaptable. UAVs are ideally suited for use in critical spray scenarios such as small fields, hilly terrain, and high-stem crops^[4,5]. According to the statistics of

Received date: 2022-12-11 **Accepted date:** 2023-04-12

Biographies: **Haiyan Zhang**, PhD candidate, research interest: precision agricultural aviation, Email: 2018200008@stu.syau.edu.cn; **Sheng Wen**, PhD, Associate Professor, research interest: smart agriculture and precision agricultural aviation, Email: vincen@scau.edu.cn; **Chunling Chen**, PhD, Professor, research interest: precision agricultural aviation application, Email: chenchunling@syau.edu.cn; **Qi Liu**, PhD candidate, research interest: precision spraying of agriculture aerial, Email: 18603030020@stumail.sdut.edu.cn; **Tongyu Xu**, PhD, Professor,

research interest: precision agricultural aviation application, Email: yatongmu@163.com; **Shengde Chen**, PhD, Associate Professor, Professor, research interest: precision agriculture aviation technology and equipment, Email: shengde-chen@scau.edu.cn.

***Corresponding author:** **Yubin Lan**, PhD, Professor, research interest: precision agricultural aviation application. Mailing address: International Laboratory of Agricultural Aviation Pesticide Spraying Technology (ILAAPST), South China Agricultural University, Guangzhou 510642, China. Email: ylan@scau.edu.cn.

the National Agricultural Technology Promotion Center of the Ministry of Agriculture and Rural Affairs, China, the number of UAVs in China reached more than 50 000, and the annual operation area reached more than 31 million hm² in 2019^[6]. After 5 years of development, the number of UAVs in China has increased by approximately 72 times, and the annual operation area has increased by approximately 108 times. Plant protection UAV spraying technology has developed into one of the primary spraying technologies in China at this stage.

Compared with ground spray application techniques, the deposition uniformity of droplets sprayed by a plant protection UAV in the crop canopy is relatively low^[7]. One reason for that is spray leakage caused by the unstable operation system of the plant protection UAV^[8]. Another possibility is that the rotor airflow field of the plant protection UAV disturbs the uniform spatial distribution of droplets, which in turn leads to uneven droplet deposition in the crop canopy. With the development of the plant protection UAV operation system, the route accuracy and stability of the plant protection UAV have been greatly improved. So the situation with regard to leakage spraying has been significantly improved. Therefore, currently, the spatial distribution of droplets under the action of the rotor airflow field is the main factor affecting the uniformity of droplet deposition.

Current studies on the rotor airflow field of UAVs have mainly focused on the distribution and development characteristics of the

rotor airflow field^[9-13], the effect of the flight parameters of UAV on the rotor airflow field^[14-18], and the influence of droplet size and the horseshoe vortex on droplet drift^[19]. However, there are relatively few studies on the droplet spatial distribution characteristics under the action of the rotor airflow field.

In order to study the spatial distribution and velocity distribution characteristics of droplets under the action of the rotor airflow field, this study simulated the rotor airflow field of plant protection UAV based on LBM and analyzed the distribution characteristics of the rotor airflow field. At the same time, the particle image velocimetry (PIV) system was selected to capture and analyze the spray field. The spatial distribution and velocity distribution characteristics of droplets were analyzed, and the effect of rotor rotation speed, nozzle position, and the distribution characteristics of the rotor airflow field on the spatial distribution and velocity distribution characteristics of droplets was revealed.

2 Materials and methods

2.1 Numerical simulation

2.1.1 UAV model

In this work, the DJI T30 six-rotor plant protection UAV (DJI-Innovations, Shenzhen, China) was selected as the numerical simulation model (Figure 1a), according to its popularity in China. The basic parameters of the UAV are listed in Table 1.

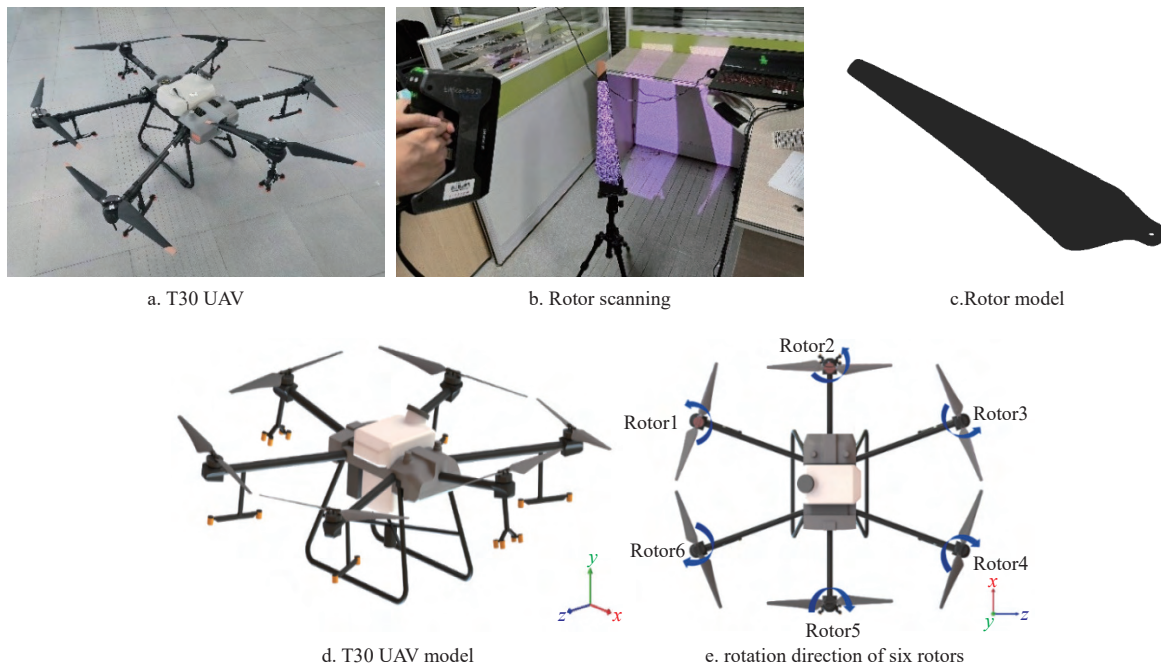


Figure 1 Modeling process of the T30 UAV

Table 1 Basic parameters of the T30 plant protection UAV

Parameter description	Value
Number of rotors	6
Rotor diameter × rotor pitch/cm ²	1158.24×609.60
Maximum wheelbase/mm ³	2858×2685×790
Cabinet volume/L	30
Standard nozzle	XR11001VS/TXVK04
Nozzle number	16

The rotor of the plant protection UAV is an extremely important part because it is the part producing the downwash airflow field, which directly influences droplet position and velocity spatial distribution. To ensure the modeling accuracy of the rotors, an automatic three-dimensional optical scanning system (EinScan Pro 2X 2020, Xianlin 3D Tech Co., Ltd., China) was used to scan the rotors with clockwise and anti-clockwise rotation. The scanning process and results are shown in Figures 1b and 1c. Then, the rotor model was reconstructed by Geomagic Studio software (Geomagic Inc., USA). The fuselage, pesticide cabinet, landing gear, and nozzles of the UAV were built by Inventor software (AutoDesk,

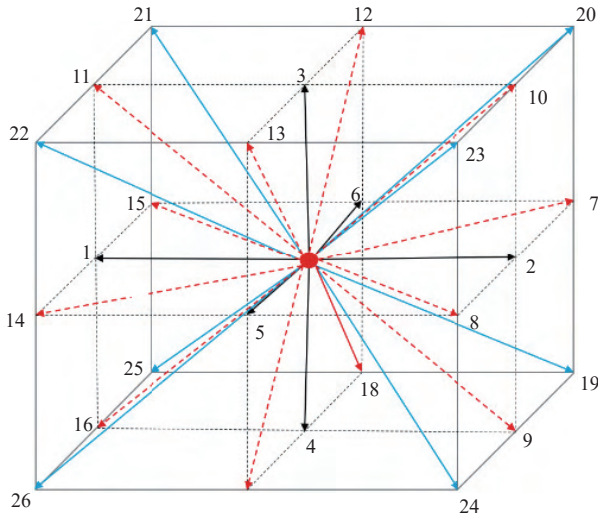
USA). The reconstructed three-dimensional model of the T30 UAV is shown in Figure 1d.

The T30 plant protection UAV has six rotors, three of which rotate clockwise (Rotors 1, 2, and 3), and the other three rotate counterclockwise (Rotors 4, 5, and 6), as shown in Figure 1e. The distribution of the UAV rotors could maintain the torque balance to allow the UAV to fly steadily.

2.1.2 Lattice Boltzmann method

The lattice Boltzmann method is based on a special discretization of the continuous Boltzmann equation. Therefore, it is a dynamic model that simulates the fluid phase at the mesoscopic level^[20]. In the lattice Boltzmann method, the computational domain is divided into a uniform Cartesian lattice. Each Cartesian lattice has a fixed number of distribution functions $f_i(x, t)$ that describe the motion and properties of the fluid and represent the probability of finding a particle at lattice position x at time t in the i -direction^[21,22].

The morphology of the lattice is defined by D dimensions and Q lattice velocity c_i . There are many velocity-space discrete schemes for 3D flow simulation, including D3Q15, D3Q19, and D3Q27. D3Q15 represents a three-dimensional lattice that has 15 lattice velocities. D3Q19 represents a three-dimensional lattice that has 19 lattice velocities. D3Q27 represents a three-dimensional lattice that has 27 lattice velocities. Although more velocities of the lattice will occupy more memory and require higher computing requirements, considering the numerical stability and accuracy of turbulent flow, the D3Q27 velocity space discrete scheme was used in this study, as shown in Figure 2.



Note: The black lines represent the discrete velocity vectors from the lattice center to the face centers of the lattice. The red lines represent the discrete velocity vectors from the lattice center to the midpoints of the lattice edges. The blue lines represent the discrete velocity vectors from the lattice center to the top corners of the lattice. D3Q27 represents a three-dimensional lattice that has 27 lattice velocities.

Figure 2 Schematic diagram of the D3Q27 lattice

By discretizing the Boltzmann equation in velocity space, physical space, and time, the lattice Boltzmann equation is given as^[23],

$$f_i(x + c_i \Delta t, t + \Delta t) = f_i(x, t) + \Omega_i(x, t) \quad (1)$$

where, Δt is the time step, s; Ω_i is the collision operator. This operator models particle collisions by redistributing particles among the populations f_i at each site.

There are many different collision operators available. In this

work, the Bhatnagar-Gross-Krook (BGK) operator with a single relaxation time was selected to discretize the lattice Boltzmann method. The BGK operator is expressed by Equation (2)^[24].

$$\Omega_i(f) = \frac{f_i - f_i^{eq}}{\tau} \Delta t \quad (2)$$

where, τ is the relaxation time, s. The lattice Boltzmann equation discretized by the BGK operator is

$$f_i(x + c_i \Delta t, t + \Delta t) = f_i(x, t) - \frac{\Delta t}{\tau} (f_i(x, t) - f_i^{eq}(x, t)) \quad (3)$$

where, f_i^{eq} is the equilibrium distribution function, and the expression is

$$f_i^{eq}(x, t) = w_i \rho \left(1 + \frac{u \cdot c_i}{c_s^2} + \frac{(u \cdot c_i)^2}{2c_s^4} - \frac{u \cdot u}{2c_s^2} \right) \quad (4)$$

where, w_i is the weight constant, and is defined as,

$$w_i = \begin{cases} \frac{8}{27}, & i = 0 \\ \frac{2}{27}, & i = 1, \dots, 6 \\ \frac{1}{54}, & i = 7, 8, \dots, 18 \\ \frac{1}{216}, & i = 19, 20, \dots, 26 \end{cases} \quad (5)$$

c_s is the sound velocity, m/s; ρ is the density of the fluid, kg/m³; u is the velocity of the fluid, m/s. ρ and u are defined as^[25],

$$\rho(x, t) = \sum f_i(x, t) \quad (6)$$

$$\rho u(x, t) = \sum c_i f_i(x, t) \quad (7)$$

2.1.3 Turbulence model

In XFlow software, the large eddy simulation (LES) approach coupled with the wall-adapting local eddy viscosity (WALE) model was employed for the simulations. The equations of the WALE model are as follows:

$$\nu_{\text{turbulent}} = \Delta^2 \frac{(G_{\alpha\beta} G_{\alpha\beta})^{3/2}}{(S_{\alpha\beta} S_{\alpha\beta})^{5/2} + (G_{\alpha\beta} G_{\alpha\beta})^{5/4}} \quad (8)$$

$$\Delta = C_w \text{Vol}^{1/3} \quad (9)$$

$$S_{\alpha\beta} = \frac{g_{\alpha\beta} + g\beta\alpha}{2} \quad (10)$$

$$G_{\alpha\beta} = \frac{1}{2} (g_{\alpha\beta}^2 + g_{\beta\alpha}^2) - \frac{1}{3} \delta_{\alpha\beta} g_{\gamma\gamma}^2 \quad (11)$$

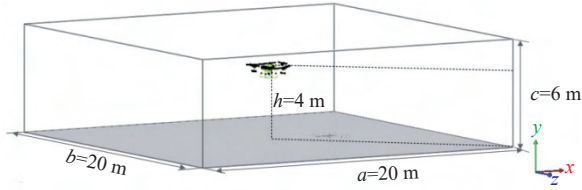
where, $\nu_{\text{turbulent}}$ is the turbulent eddy viscosity, Pa·s; Δ is the filter scale; $G_{\alpha\beta}$ and $S_{\alpha\beta}$ are the strain rate tensors of the resolved scales; C_w is a constant with a value of 0.2. Vol is the grid volume; $g_{\alpha\beta}$, $g_{\beta\alpha}$, and $g_{\gamma\gamma}$ are the strain rate tensor; $\delta_{\alpha\beta}$ is the Kronecker symbol.

2.1.4 Computational domain and spatial discretization

In this work, the downwash airflow of the DJI T30 plant protection UAV in hover was simulated. To analyze the effect of the rotors' rotation speed on the downwash airflow distribution, three rotation speeds are set in this study: 1000 r/min, 1500 r/min, and 1800 r/min.

The virtual wind tunnel is selected as the computational domain for simulation. The size of the virtual wind tunnel was 20 m×6 m×20 m in the X , Y , and Z directions, respectively. The UAV was placed in the center of the virtual wind tunnel. The height of the UAV from the ground is 4 m. The detailed sizes are shown in Figure 3. The simulation lasted 3 s with a time step of 0.005 s. When the computation ran for 3 s, the downwash airflow was fully

dispersed^[26].



Note: a , b , and c are the length, width, and height of the virtual wind tunnel, respectively. h is the distance from the UAV to the ground.

Figure 3 Schematic diagram of the computational domain

The aim of the simulation is to obtain the downwash airflow field of the UAV. The rotor generates the downwash airflow field. Therefore, to guarantee that the downwash airflow develops accurately and steadily, the discretization resolutions of the six rotors and the wake were set to 0.025 m and 0.0125 m, respectively. The fuselage and nozzle have little effect on the downwash airflow field; thus, the fuselage, nozzle, and global spatial resolutions were set to 0.1 m. In the limitation of the computer resource, this discretization resolution combination can provide a more accurate and steady downwash airflow field, as well as acceptable computational efficiency. The simulation refinement is shown in Figure 4.

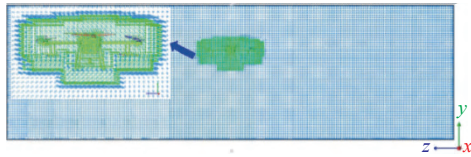


Figure 4 Lattice distribution using the adaptive wake refinement strategy



a. Two-phase-flow visualization system and ultrasonic anemometer

2.2 Numerical simulation accuracy evaluation

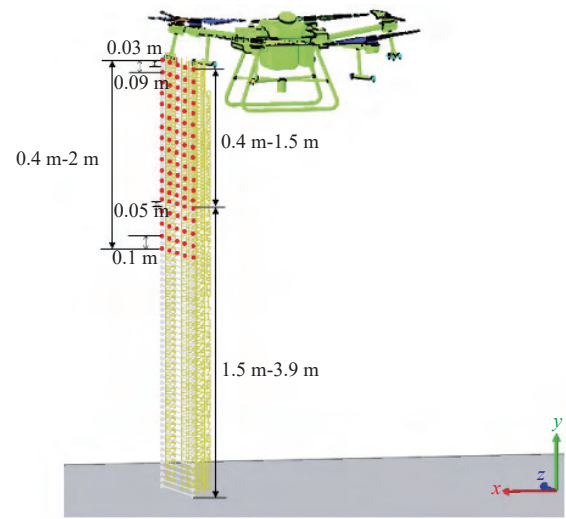
The rotor airflow velocities of the numerical simulation and actual UAV in hover were measured at a rotor rotational speed of 1000 r/min. The error range of the rotor airflow velocities obtained by the two methods was compared to evaluate the accuracy of the numerical simulation results.

2.2.1 Experimental setup

To obtain a safe and steady rotor downwash airflow field, the rotor of DJI T30 was removed and mounted on the two-phase flow visualization system. Then, the ultrasonic anemometer produced by Jinzhou Tiannuo Huaneng Instrument Co., Ltd., China was selected to measure the airflow velocity formed by the rotor mounted on the two-phase flow visualization system. The airflow velocity measurement range is 0-60 m/s. The measurement accuracy is ± 0.2 m/s, or 2% of the reading, whichever is greater. The resolution is 0.1 m/s.

The abovementioned two-phase flow visualization system mainly consists of the rotor system, spray system, control system, and lifting and walking device. These systems can be used to form the downwash airflow field of the UAV and the spray field with or without the rotor downwash airflow field, as shown in Figure 5a. The width of the two-phase flow visualization system is 4 m. The initial height of the rotor system is 1.8 m from the ground, which can be adjusted within 0-1 m by a remote control lifting device. The rotor rotational speed can be adjusted within 600-2500 r/min. The tilt angle of the UAV can be adjusted within the range of -30° - 30° . The spray system supports hydrodynamic and centrifugal atomization. The spray pressure range is 0-1.2 MPa. The flow rate range is 0-2 L/min. The spraying time is freely controlled by the operator.

In this experiment, the rotor system was adjusted to its highest position of 2.8 m above ground.



b. Distribution diagram of sampling points

Figure 5 Two-phase-flow visualization system and airflow velocity measurement distribution map

2.2.2 Airflow velocity acquisition method

To collect the rotor airflow velocity at different positions in the rotor downwash airflow field, 62 velocity sensor lines were set below Rotor 2. The first line was set at 0.40 m below Rotor 2. The last line was 3.90 m below Rotor 2. The interval between adjacent velocity sensor lines was 0.03 m for 0.40-1.50 m below Rotor 2 where the spray field was obtained and 0.05 m for 1.50-3.90 m below Rotor 2. The length of the velocity sensor line was equal to the rotor diameter. Every velocity sensor line included 100 equally spaced measurement points. The arrangement of the velocity sensor

lines below Rotor 2 is shown in Figure 5b.

To reduce the measurement risk and effort, the interval of the vertical measurement point was set to 0.09 m within 0.40-1.50 m below the rotor and to 0.10 m within 1.50-2.00 m below the rotor when the ultrasonic anemometer was used to measure the airflow velocity of the downwash airflow field. The interval of the radial measurement point was 0.25 m. The detailed distribution of the measurement points is shown in Figure 5b.

The average airflow velocity at different heights or radial positions of the rotor was calculated by Equations (12) and (13).

$$V_{Ra} = \frac{\sum_{j=1}^{62} V_{Ha-j}}{62} \tag{12}$$

$$V_{Hj} = \frac{\sum_{a=1}^{100} V_{Rj-a}}{100} \tag{13}$$

where, V_{Ra} is the average airflow velocity for rotor radial position number a , m/s; V_{Ha-j} is the airflow velocity at the radial position of rotor i and height j , m/s; V_{Hj} is the average airflow velocity at height j below the rotor, m/s; V_{Rj-a} is the airflow velocity below the rotor at height j and radial number a , m/s.

2.3 PIV experiment

2.3.1 Experimental Program

There are two experimental variables, namely, the rotor rotational speed with 4 values of 0, 1000 r/min, 1500 r/min, and 1800 r/min, and the nozzle position with 4 values of 0, 0.20 m, 0.35 m, and 0.50 m from the motor. The schematic layout of the nozzle position is shown in Figure 6.

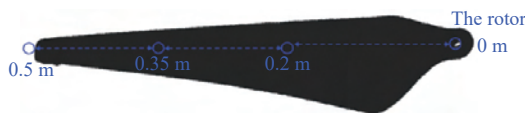


Figure 6 Schematic layout of the four nozzle positions

To generate a safe and steady rotor downwash flow field and spray field, a two-phase-flow visualization system was used to simulate the rotor downwash airflow field and the spray field. To guarantee that the two-phase-flow visualization system accurately replicated the downwash airflow field of the T30 UAV in the hover and spray fields, the original rotor and the standard nozzle with TXVK-04 (TeeJet Technologies (Tianjin) Co., Ltd.) of the T30 UAV were mounted on the two-phase flow visualization system to form the rotor downwash flow field and spray field. Additionally, the vertical distance between the nozzle and the rotor was 0.42 m.

2.3.2 Spray field acquisition method

To illuminate the spray field, a dual-cavity Nd:YAG laser (shown in Figure 7) was used to continuously emit two laser pulses, which were expanded into a two-dimensional laser sheet by a cylindrical lens in the light-guiding arm. The light-guiding arm was placed at 1 m from the nozzle. The angle of the light-guide arm was adjusted until the two-dimensional laser sheet coincided with the

central sheet of the spray field.



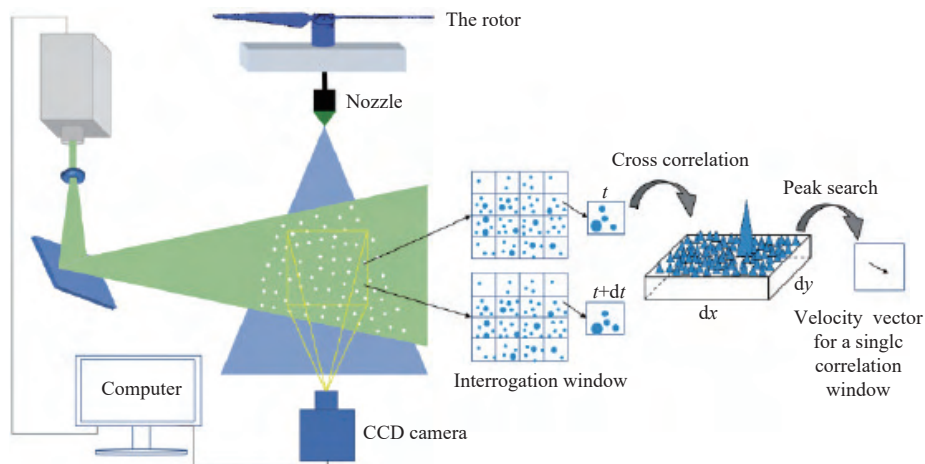
Figure 7 Particle image velocimetry (PIV) system

A Charge Coupled Device (CCD) camera was placed at 1.12 m in front of the nozzle, aligned at 90° to the laser sheet, and focused on the central sheet of the spray field, as shown in Figure 7. A 425.21 mm×425.21 mm view field was formed at this distance between the camera and the nozzle. To guarantee that each droplet in the spray field photographed by the camera has a clear outline and an appropriate threshold value that could ensure that the post-processing software can identify the droplet accurately, the laser pulse energy was set to 285 mJ. The time between two laser pulses was optimized and finally set to 50 μs. The emission frequency of the laser pulse was set to 7.5 Hz. Two hundred pairs of images were continuously recorded for each experimental treatment.

In this work, the spray field within 1.2 m below the rotor (within 0.8 m below the nozzle) needed to be captured. Due to the limitation of the camera resolution, the maximum photograph area of the camera is 500 mm×500 mm; thus, the 0.8 m spray field needed to be captured twice. Completing the calibration of the PIV system, the rotor and spray systems were turned on. When the downwash airflow field of the UAV and the spray field were stabilized, the PIV system was activated and used to record the spray field. After the first section of the spray field was recorded, the rotor and spray systems were turned off. The rotor system was raised by 0.4 m. Then, the rotor and spray systems were turned on again. After the rotor downwash airflow field and spray field were stabilized, the PIV system was activated to record the second section of the spray field.

2.3.3 Spray field post-processing method

The 200 pairs of spray field images were imported into the post-processing software of the PIV system, namely, INSIGHT 4G software. A new background was formed by calculating the average



Note: “ t ” is the time that was recorded for the first frame of the spray flow field. “ $t+dt$ ” is the time that was recorded for the second frame of the spray flow field. dx and dy are the displacements of the droplet in the x and y directions respectively, in the interrogation window.

Figure 8 Schematic diagram of spray field recording and analysis

intensity of 200 pairs of images. Two hundred pairs of higher-quality images were generated by subtracting the new background. Then, the Nyquist grid processor with an interrogation window size of 32×32 pixels or 48×48 pixels was used to divide the new 200 pairs of spray field images. The cross-correlation and adaptive cross-correlation algorithms were applied to analyze the image pairs and generate the vector fields of the spray field. Global and local vector validation algorithms were selected to validate the vector field, namely, to identify and remove the bad vectors and interpolate the new vector from the valid neighbors.

The droplet velocity was low when the rotor system was not activated. However, the droplet velocity was high when the rotor system was activated. Therefore, droplet displacement at the same time interval was extremely different with or without the rotor downwash airflow field. Moreover, the droplet concentration was lower when the rotor system was turned on. To ensure that there was an appropriate droplet concentration and displacement in the interrogation window, the interrogation window size was set to 32×32 pixels when the rotor was turned off and to 48×48 pixels when the rotor system was turned on.

3 Results and discussion

3.1 Validation of results

To evaluate the accuracy of the simulation model in this work, the rotor airflow velocities obtained by the two methods were measured, and the results are shown in Figure 9. Figure 9 shows that the errors of the rotor airflow velocities generated by the two methods were basically within 10%. Only the errors of the airflow velocities at the sample points of 1.9 m and 2.0 m below the rotor were more than 10%, which occurred possibly because the airflow

velocities were affected by the ground effect of airflow. In total, the accuracy of the numerical simulation results was high, and the numerical simulation results can be used for further analysis of the distribution and development characteristics of the downwash airflow field.

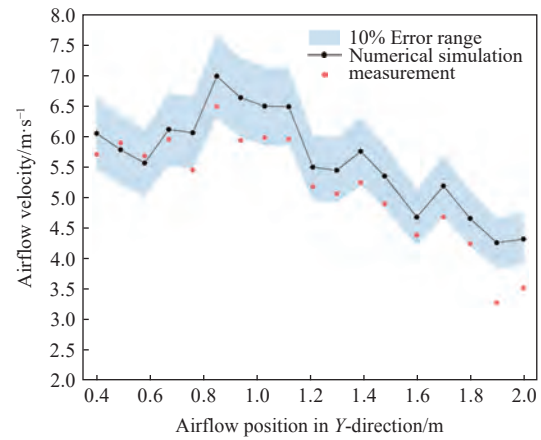


Figure 9 Comparison of airflow velocity measured by two methods

3.2 UAV rotor airflow field

After the airflow passed through the surface of the high-speed rotating rotor, a circular vortex was formed, and the circular vortex spread downward in accordance with the “dispersion-shrinkage-redispersion” rules, as shown in Figure 10. The development and distribution characteristics of the rotor downwash airflow field at three rotational speeds were similar.

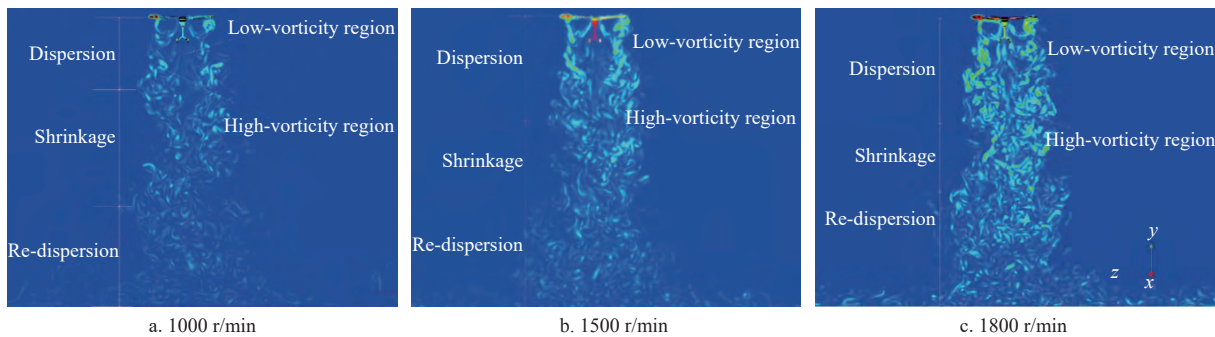


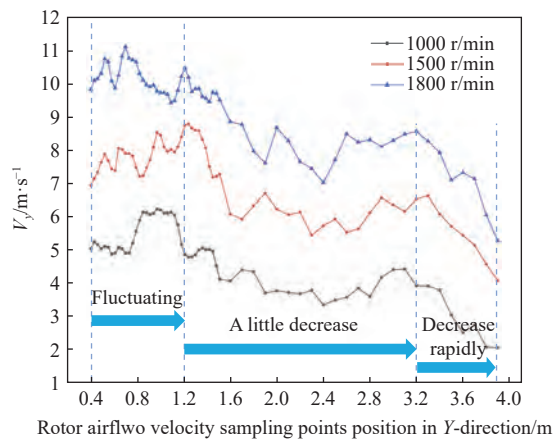
Figure 10 Average vorticity distribution at different rotor rotation speeds

In the initial dispersion stage of the rotor downwash airflow field, there were clear high-vorticity and low-vorticity regions in the rotor downwash airflow field (shown in Figure 10). The high-vorticity airflow was mainly concentrated in the middle region of the rotor. The average airflow vorticities of the high-vorticity regions at rotor rotational speeds of 1000 r/min, 1500 r/min, and 1800 r/min were 85.47 s⁻¹, 129.28 s⁻¹, and 163.66 s⁻¹, respectively. The low-vorticity rotor airflow was mainly concentrated below the motor (shown in Figure 10). At three different rotor rotational speeds, the average airflow vorticities of the low-vorticity region were 58.34, 100.49, and 107.76, respectively. These values were significantly lower than the average vorticities of the abovementioned high-vorticity region. The different vorticity airflow perturbs the spray field and disperses the droplets differently. The non-uniform distribution of vorticity in the rotor downwash airflow field will lead to a more nonuniform distribution of droplets and droplet velocity below the rotor, which in turn

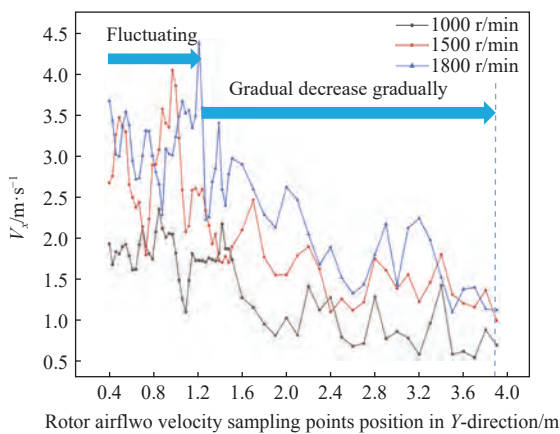
affects the uniformity of droplet deposition in the target area.

Figure 11a shows the variation curves of the Y-directional airflow velocity with its dispersion distance in the Y-direction. The Y-directional airflow velocity fluctuated without showing an obvious trend of rising or falling before 1.20 m under the rotor. When the rotor airflow developed to 3.20 m below the rotor, the Y-directional airflow velocity showed a slight decrease. The Y-directional airflow velocity at 3 rotor rotational speeds of 1000, 1500, and 1800 r/min decreased by 0.58, 1.10, and 1.03 m/s, respectively. However, above 3.20 m from the rotor, the Y-directional airflow velocity started to rapidly decrease (shown in Figure 11a). Within the distance of 0.90 m, the Y-directional rotor airflow velocity at 3 rotor rotational speeds decreased by 2.37, 2.09, and 3.20 m/s.

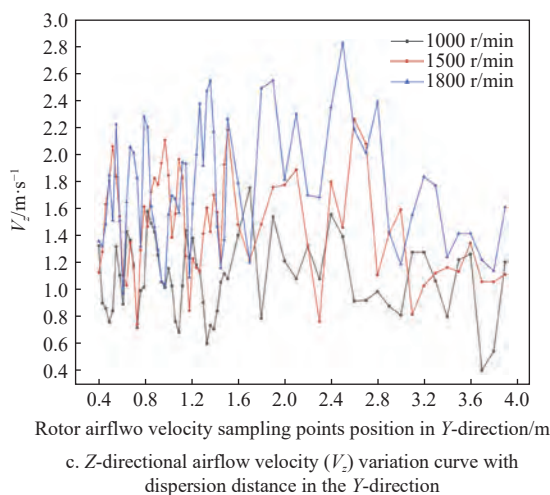
The X-directional airflow velocity was also not steady before 1.2 m under the rotor. At 1.2-3.9 m under the rotor, the X-directional airflow velocity gradually decreased as the Y-directional



a. Y-directional airflow velocity (V_y) variation curve with dispersion distance in the Y-direction



b. X-directional airflow velocity (V_x) variation curve with dispersion distance in the Y-direction



c. Z-directional airflow velocity (V_z) variation curve with dispersion distance in the Y-direction

Note: the Y-, X-, and Z-directional airflow velocities are the fractional velocities of the airflow velocity in the X-, Y-, and Z-directions.

Figure 11 V_y , V_x , and V_z variation curves with their dispersion distance in the Y-direction

distance increased, as shown in Figure 11b. In total, from 0.4 to 3.9 m below the rotor, the X-directional rotor airflow velocity decreased by 63.86%, 62.67%, and 69.35% when the rotor rotational speed was 1000 r/min, 1500 r/min, and 1800 r/min, respectively. The Z-directional rotor airflow velocity fluctuated and did not show an evident trend, as shown in Figure 11c.

In summary, according to the development characteristics of the rotor airflow velocity in the X and Y directions with its diffusion distance, this study recommended that the flight height of the T30

plant protection UAV should not exceed 3.2 m. On the one hand, the UAV flight height increases, the droplet transportation distance increases, and the risk of droplet drift increases. Moreover, the Y-directional rotor airflow velocity started to rapidly decrease beyond 3.2 m, and the ability to assist droplets to transport downward rapidly decreased, which also caused the risk of droplet drift to increase. On the other hand, the rotor airflow velocity in both the Y- and X- directions outside 3.2 m was relatively low, and the disturbance ability to crop branches was relatively weak, especially for sturdy branch crops such as maize. This will reduce the penetration probability of droplets within the crop canopy.

The rotor airflow velocity distribution along the rotor radial direction determines the nozzle installation position and affects the distribution of the spray field. In this study, based on the velocity sensor line described in Section 2.2, the rotor airflow velocity in the X, Y, and Z directions was collected in the rotor downwash airflow field. The distribution curves of the rotor airflow velocity along the rotor radial direction in the three directions are shown in Figure 12.

As shown in Figure 12a, the distribution curves of the Y-directional rotor airflow velocity along the rotor radial direction resembled an inverted 'W'. Namely, from the motor to the rotor tip, the Y-directional rotor airflow velocity tended to increase first and then decrease. In the left rotor downwash airflow field, the maximum Y-directional rotor airflow velocity occurred between -0.24 and -0.26 m from the motor for 3 rotor rotational speeds. In the right rotor downwash airflow field, the maximum Y-directional rotor airflow velocity occurred between 0.15 and 0.21 m from the motor. The maximum average Y-directional airflow velocities at rotor rotational speeds of 1000 r/min, 1500 r/min, and 1800 r/min were 8.90 m/s, 12.01 m/s, and 15.64 m/s, respectively. Additionally, the Y-directional rotor airflow velocity was lower for the region of -0.11 -0.04 m, and the average Y-directional rotor airflow velocity in this region was 4.90 m/s, 7.60 m/s, and 9.24 m/s at 3 rotor rotational speeds.

The distribution curves of the X-directional rotor airflow velocity along the rotor radial direction were similar to those of the Y-directional rotor airflow velocity, which were the inverted "W" type, as shown in Figure 12b. When the rotor rotational speed was 1800 r/min, the X-directional airflow velocity in the left rotor downwash airflow field basically reached the maximum value at -0.19 m, and the maximum value covered a large area, which generally ended at -0.45 m. The average X-direction airflow velocity in the abovementioned range was 3.93 m/s. The maximum X-directional airflow velocity in the right rotor downwash airflow field was in the range of 0.15-0.33 m, with a maximum velocity value of 4.15 m/s. When the rotor rotational speed was 1500 r/min, the maximum X-directional airflow velocity in the left rotor downwash airflow field was approximately -0.4 m from the motor, with a maximum velocity value of 3.85 m/s. In the right rotor downwash airflow field, the X-directional airflow velocity curve had two peaks at distances of 0.13 and 0.32 m from the motor. The maximum X-direction airflow velocities were 3.98 m/s and 4.30 m/s, respectively. When the rotor rotational velocity was 1000 r/min, the maximum X-direction airflow velocity on the left rotor downwash airflow field was at the same position as that at 1500 r/min, and the maximum X-direction airflow velocity was 2.94 m/s. In the right rotor downwash airflow field, the maximum X-direction airflow velocity was between 0.12 and 0.42 m. The X-directional airflow velocity in this range was relatively high, with an average of 2.28 m/s. The position of the maximum X-directional airflow velocity described above basically coincides with the high vorticity

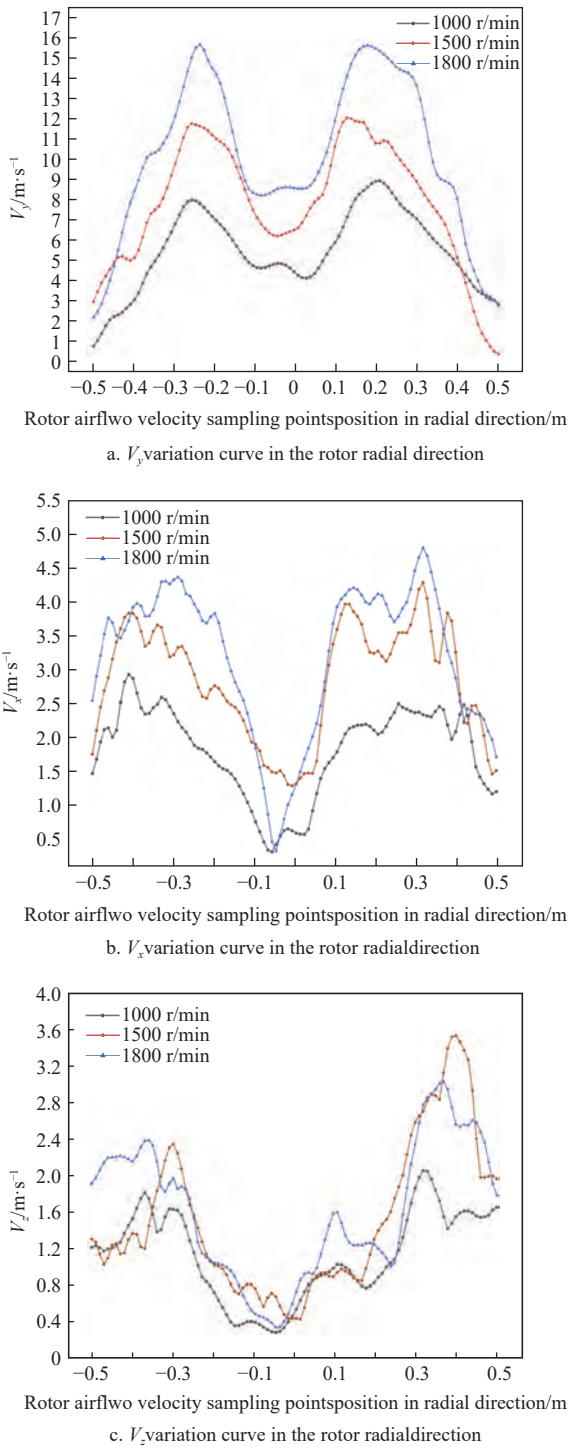


Figure 12 V_y , V_x , and V_z variation curves in the rotor radial direction

region.

The distribution curves of the Z-directional rotor airflow velocity along the rotor radial direction were also irregularly inverted 'W'. The Z-directional rotor airflow velocities were much lower than those of the other two directions. The larger Z-directional rotor airflow velocity was basically concentrated at 0.32-0.40 m from the motor. The Z-directional rotor airflow velocity within 0.2 m to the left and right of the motor was relatively lower, as shown in Figure 12c.

3.3 Spray velocity field

Due to the sudden injection of high-speed liquid into the air, the original dispersion state of the air was broken, which caused the air pressure difference and produced self-induced vortices in the spray field. The air self-induced vortex coupled with the spray field generates multiple scales of local vortices in the spray field and affects the spatial distribution of droplets, as shown in Figure 13a.

As shown in Figure 13a, many droplets were concentrated in the middle region of the spray field, and the droplet size in this region was small when the rotor system was not activated. The droplet concentration was relatively low at the edge of the spray field, and the droplet size was larger. This phenomenon occurs mainly because small droplets follow airflow more easily; thus, the induced vortices continued to transport the small droplets to the central region of the spray field. Additionally, the induced vortices' centrifugal force propelled large droplets to the edge of the spray field. As a result, the droplet concentration decreased and the droplet size increased as the distance from the central axis of the spray flow field increased, as previously mentioned.

When the rotor system was activated, the rotor downwash the airflow field coupled with the spray field, breaking the original dispersion of the droplets and redistributing the droplets in space. Figures 13b-13d and 14a depict the droplet spatial distribution and the radial distribution curve of droplet concentration (the number of droplets per square centimeter) when the nozzle was installed below the motor. Comparing Figures 13a and 13d, it was found that the rotor downwash airflow field caused the nozzle atomization angle, droplet concentration, and spray field width to decrease, but the vortex scale in the spray field increased. Moreover, as the rotor rotational speed increased, the nozzle atomization angle, droplet concentration, and spray field width decreased, while the vortex scale in the spray field increased, as shown in Figure 13. Additionally, the average droplet concentration fell by 36.93%, 54.43%, and 68.09% at rotor rotational speeds of 1000 r/min, 1500 r/min, and 1800 r/min, respectively, in comparison to no rotor downwash airflow field. The droplet concentration was essentially symmetrically distributed when the nozzle was mounted below the motor because the rotor downwash airflow field coupled with the spray flow field was symmetrical, as displayed in Figure 14a.

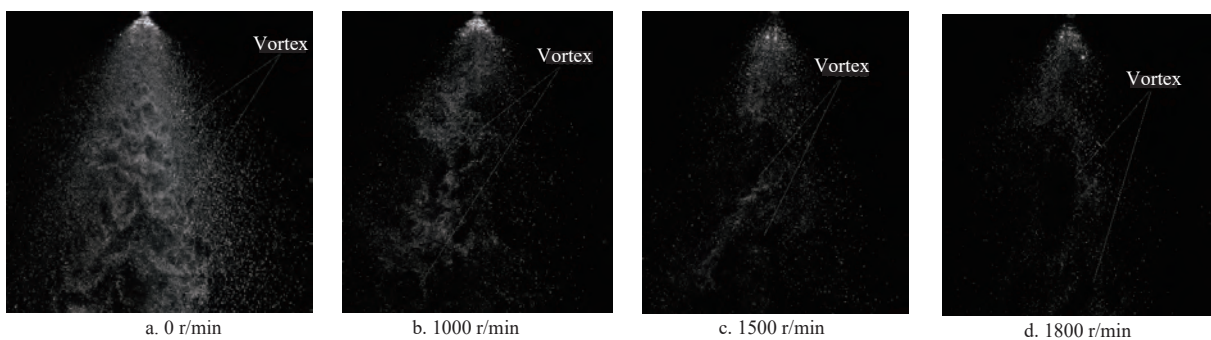


Figure 13 Droplet spatial distribution at different rotor rotation speeds

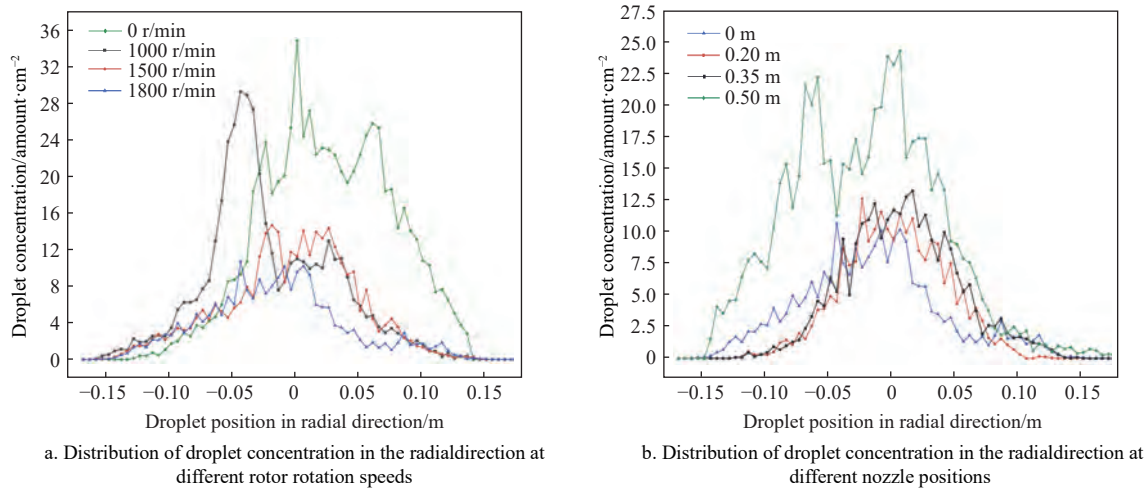


Figure 14 Distribution of droplet concentration at different rotor rotation speeds or nozzle positions

When the nozzle was positioned at various positions below the rotor, the radial distribution curves of the droplet concentration and droplet spatial distribution are shown in Figures 14b and 15, respectively. As previously noted, the rotor downwash airflow field distribution was symmetrical. Therefore, the spray field was also symmetrically distributed under the symmetrical rotor downwash airflow field when the nozzle was installed below the motor, as shown in Figure 13d. When the nozzle was installed at 0.2 m from the motor, the rotor airflow coupling with the right-half spray field was stronger, as shown in Figure 16. Therefore, the droplets

originally in the left-half spray field moved to the right-half spray field, which resulted in a very low droplet concentration in the left-half spray field. Because the rotor airflow velocity was close to the maximum at 0.20 m from the motor, the maximum rotor airflow velocity resulted in the strongest perturbation on the spray field, the lowest droplet concentration, the narrowest spray field width, and the most asymmetric droplet spatial distribution in which the droplet concentration in the right-half spray field was greater than that in the left-half spray field, as shown in Figure 15a.

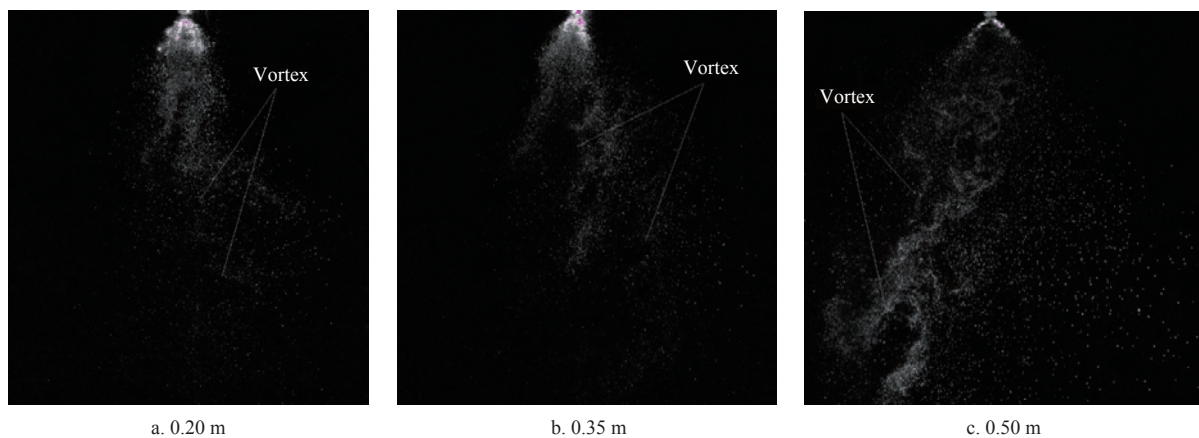


Figure 15 Droplet spatial distribution at different nozzle positions

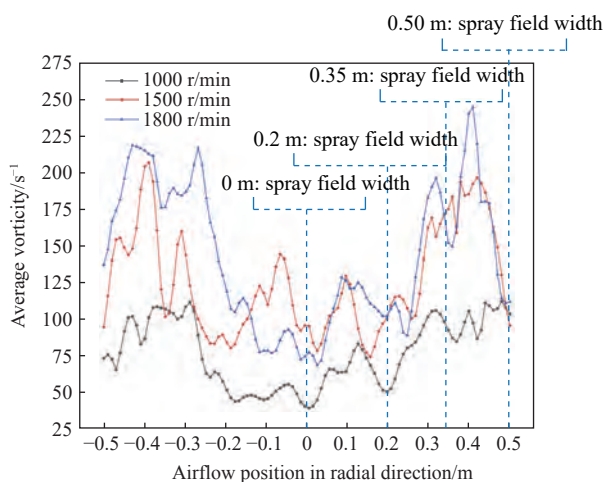


Figure 16 Area vorticity distribution in radial direction

When the nozzle was installed at 0.35 m from the motor, the vorticity of the rotor airflow coupling with the right-half spray field was still higher than that with the left-half spray field, as shown in Figure 16; thus, the rotor airflow coupling with the right-half spray field had a stronger ability to induce the droplets to move to the right, especially small droplets. Therefore, when the nozzle was installed at 0.35 m from the motor, the droplet concentration in the spray field was asymmetric, and the droplet concentration in the right-half spray field was greater than that in the left-half spray field. Additionally, the droplet concentration in the right-half spray field slightly increased, and the boundary of the right spray field was clearly expanded, as shown in Figure 15b.

Only the left-half spray field was situated near the edge of the rotor downwash airflow field when the nozzle was installed at 0.50 m from the motor (the rotor wing tip). Many droplets were

transferred to the left-half spray field due to the vortices at the edge of the rotor downwash airflow field, which resulted in a non-uniform droplet distribution in the spray field, as shown in Figure 15c. The droplet concentration in the left-half spray field was significantly higher than that in the right-half spray field and noticeably higher than the droplet concentration under the circumstances of the other three nozzle positions, as shown in Figure 14b.

Figure 17 shows the average velocity field at different rotor rotational speeds when the rotor was installed below the motor. When the rotor system was not activated, the droplet velocity field was symmetrical along the nozzle center axis, as shown in Figures 17a. Additionally, the fluid was atomized into many small droplets under the action of external force. The droplet was affected by air

resistance during the downward movement; thus, some droplet velocities decayed faster. These low-velocity droplets easily converged to form a larger droplet. Under the effect of the induced vortices' centrifugal force, these larger droplets were thrown to the edge of the spray field. Therefore, the droplet velocity near the spray field's center axis was higher, while the droplet velocity toward the spray field's edge was lower.

When the rotor system was activated, the droplet velocity in the spray field significantly increased, as shown in Figure 17. At 1.2 m below the rotor, the average droplet velocities at 0, 1000 r/min, 1500 r/min, and 1800 r/min were 1.27, 6.64, 9.12, and 10.29 m/s, respectively. The droplet velocity increased by 422.83%, 618.11%, and 710.24% when the rotor rotation speed rose from 0 to 1000, 1500, and 1800 r/min, respectively.

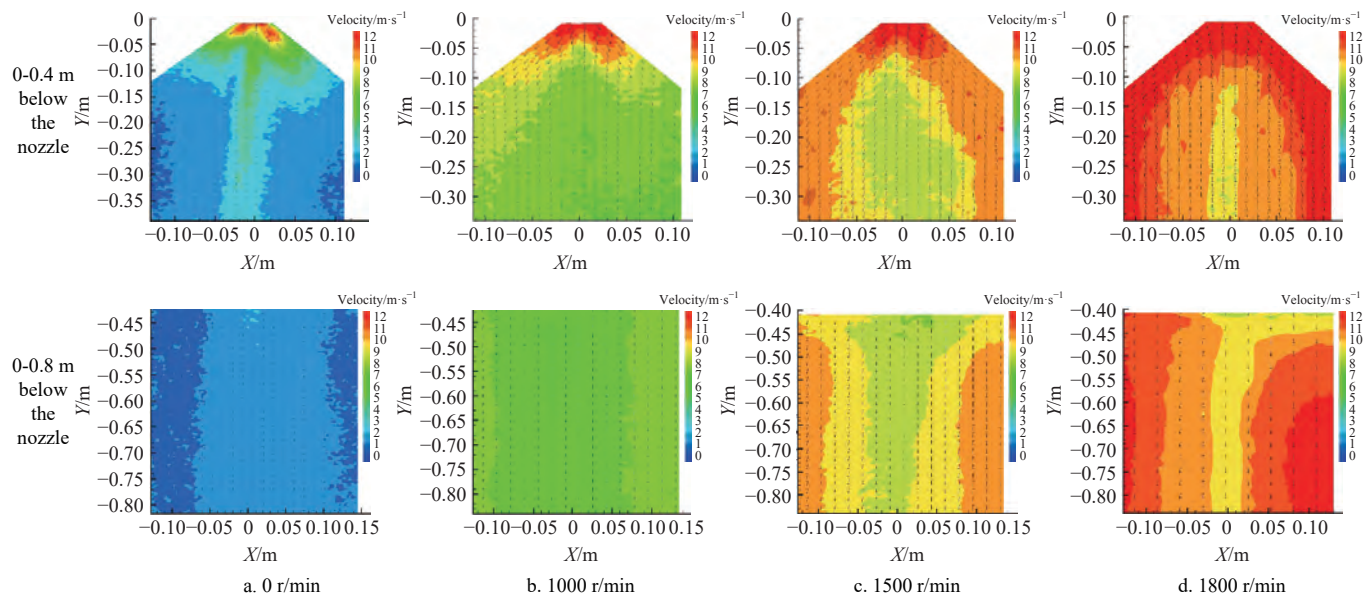


Figure 17 Average droplet velocity field at different rotor rotation speeds (0.4 MPa)

When the rotor was installed below the motor, the droplet velocity radial distribution was also symmetrical under the effect of the symmetrical airflow, as shown in Figures 17d. Moreover, the airflow velocity coupled with the spray field increased as the radial distance increased; thus, the droplet velocity increased from the center axis to the boundary of the spray field.

The Y-direction rotor airflow velocity was the highest, and the rotor airflow velocity coupled with the spray field decreased as the radial distance of the nozzle increased at 0.20 m from the motor, as shown in Figure 12a. However, within 0.10 m radially of the nozzle, the rotor airflow velocity coupling with the left-half spray field decreased by 1.5 m/s, while the rotor airflow velocity coupling with the right-half spray field decreased by 4.6 m/s. As a result, when the nozzle was installed 0.20 m from the motor, the droplet velocity was not affected by the decrease in the rotor airflow velocity, and the droplet velocity in the left spray field was basically the same. The droplet velocity in the right spray field decreased with the decrease in the rotor airflow velocity. For this reason, the droplet velocity field shown in Figures 18a were asymmetric, and the droplet velocity in the left-half spray field was faster than that in the right-half spray field.

When the nozzle was installed at 0.35 m from the motor, the rotor airflow velocity coupling with the left-half spray field increased as the radial distance of the nozzle increased, while the rotor airflow velocity coupling with the right-half spray field

decreased with the increase in the radial distance of the nozzle. This resulted in an asymmetrical droplet velocity field where the droplet velocity in the left-half spray field was significantly larger than the droplet velocity in the right-half spray field, as shown in Figures 18b.

When the nozzle was installed at 0.50 m from the motor, the spray field was essentially out of the rotor downwash airflow field. Only the left-half spray field was affected by the rotor downwash airflow field; thus, the droplet velocity in the left-half spray field slightly increased. However, the overall droplet velocity was low, only slightly higher than the droplet velocity when the rotor system was closed, as shown in Figure 18c.

In summary, compared with the droplet velocity without the rotor downwash airflow field, the droplet velocity significantly increased when the rotor system was activated. The droplet velocity increased as the rotor rotational speed increased. The droplet velocity radial distribution was consistent with the rotor airflow velocity radial distribution. Based on the radial distribution of rotor airflow velocity and droplet velocity, it is recommended to install the nozzle below the motor or at 0.20 m from the motor. The droplet velocity under this nozzle position combination is the largest, and the droplet spatial distribution and velocity distribution are relatively uniform. This is conducive to droplets moving downward, reducing drift, and increasing droplet deposition uniformity.

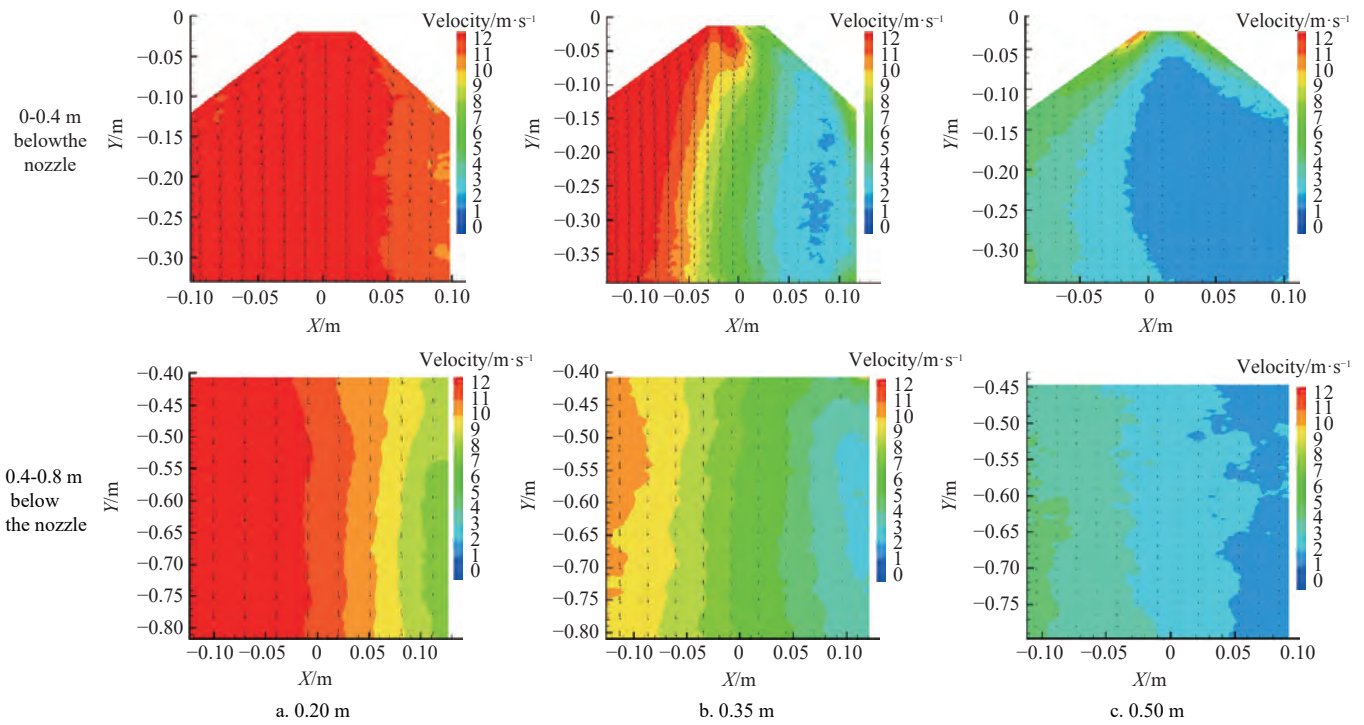


Figure 18 Average droplet velocity field at different nozzle positions (1800 r/min and 0.4 MPa)

3.4 Regression model of droplet velocity and airflow velocity or transportation distance of droplet

3.4.1 Regression model of droplet velocity and airflow velocity in the Y-direction

Based on the analysis in Section 3.3, it is known that the rotor downwash airflow field has an extremely significant effect on the droplet velocity and is the dominant factor affecting the droplet velocity. In actual research, the measurement cost of rotor airflow velocity is relatively low, and the measurement cost of droplet velocity is very high; thus, it is a more economical method to establish the relationship model between droplet velocity and rotor

airflow velocity and predict the droplet velocity based on the model and rotor airflow velocity. In this study, a conventional linear regression model was established based on the rotor airflow velocity obtained from the numerical simulation and the droplet velocity measured by the experimental method, as shown in Figure 19. The R^2 of the regression model between the droplet velocity and the rotor airflow velocity was 0.8250, 0.8335, and 0.7034 when the rotor rotational speed was 1000 r/min, 1500 r/min, and 1800 r/min, respectively. This indicates that the regression model between the rotor airflow velocity and the droplet velocity established in this study can be used for droplet velocity prediction.

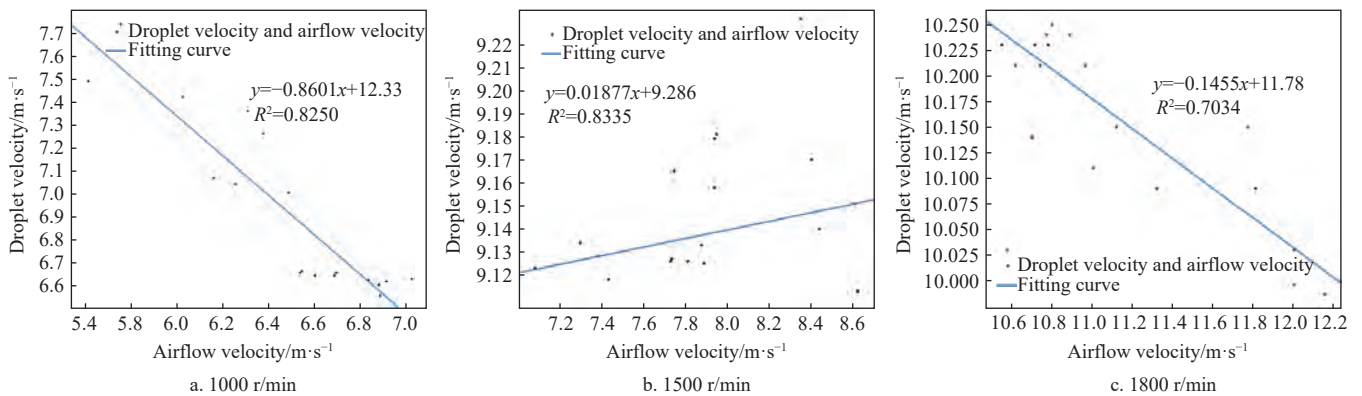


Figure 19 Regression model of droplet velocity and airflow velocity

3.4.2 Regression model of droplet velocity and transportation distance of droplet

A conventional regression model of droplet velocity and its moving distance in the Y direction was constructed based on the droplet velocity data within 1.20 m below the rotor at 0, 1000, 1500, and 1800 r/min, as shown in Figure 20. The R^2 values of the regression model at rotor rotational speeds of 0, 1000, 1500, and 1800 r/min are 0.9990, 0.9969, 0.9868, and 0.9668, respectively. This indicates that these regression models can be used to predict the droplet velocity of the T30 plant protection UAV at different heights.

4 Conclusions

The computational fluid dynamics based on the LBM was used to simulate the downwash airflow field of the DJI T30 six-rotor plant protection UAV. The PIV system was selected to capture the spray field with and without the rotor downwash airflow field. Analyzing the distribution of the downwash airflow field of the UAV and spray field with and without the rotor downwash airflow field, some conclusions are summarized below:

1) The rotor downwash airflow field exhibited the ‘dispersion-shrinkage-dispersion’ development rule. In the initial dispersion

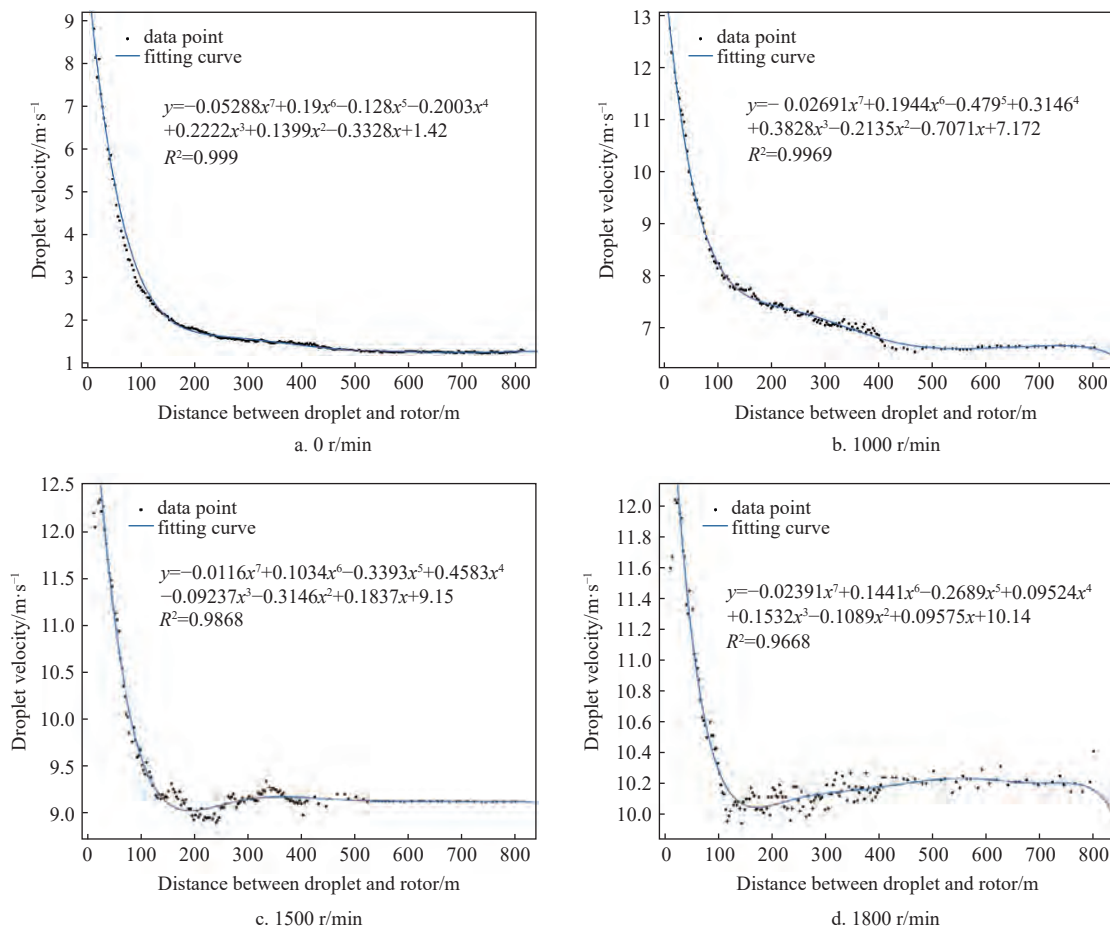


Figure 20 Regression model of droplet velocity and its transportation distance

stage of rotor airflow, there were clear high-vorticity and low-vorticity areas in the rotor downwash airflow field, with the low-vorticity airflow primarily concentrated below the motor and the high-vorticity airflow mainly focused in the central area of the rotors.

2) In the initial dispersion stage of the rotor airflow, the *Y*-directional airflow velocity fluctuated without indicating an obvious trend of decreasing or increasing before 1.20 m under the rotor. When the rotor airflow developed to 3.20 m below the rotor, the rotor airflow velocity in the *Y*-direction showed a slight decrease. After 3.20 m from the rotor, the airflow velocity in the *Y*-direction started to slow drastically. Therefore, it is recommended that the DJI T30 plant protection UAV should not exceed 3.20 m in flight height during field spraying operations.

3) The radial distributions of the *X*, *Y*, and *Z*-directional rotor airflow velocities were relatively similar and exhibited inverted ‘W’-type distributions. From the motor to the rotor tip, the airflow velocity tended to initially increase and then decrease. The maximum rotor airflow velocity in the *Y*-direction appeared at 0.15–0.25 m from the motor, and the maximum *Y*-directional airflow velocity was 15.64 m/s when the rotor rotational speed was 1800 r/min.

4) The rotor downwash airflow field caused the nozzle atomization angle, droplet concentration, and spray field width to decrease while the vortex scale in the spray field increased. Additionally, as the rotor rotational speed increased, the vortex scale expanded, and the nozzle atomization angle, spray field width, and droplet concentration decreased. Compared to the droplet concentration without a downwash airflow field, the average droplet concentration decreased by 36.93%, 54.43%, and 68.09% at rotor

rotational speeds of 1000, 1500, and 1800 r/min, respectively.

5) When the nozzle was installed in various radial locations below the rotor, the droplet spatial distribution and velocity distribution were completely different. When the nozzle was installed directly below the motor, the droplet spatial distribution and velocity distribution in the spray field were relatively symmetrical. From the spray field center axis to the spray field edge, the droplet concentration gradually decreased, and the droplet velocity increased. When the nozzle was installed at 0.20 m and 0.35 m from the motor, the droplets clearly moved toward the right under the induction of stronger rotor vortices. This resulted in a higher droplet concentration in the right-half spray field than in the left-half spray field. However, the droplet moved toward the left when the nozzle was installed in the rotor tip. For four nozzle positions, when the nozzle was installed at 0 or 0.20 m from the motor, the droplet average velocity was quite high. However, the droplet average velocity was slower when the nozzle was installed in the other two positions. Therefore, it is recommended that the nozzle is installed at 0 or 0.20 m from the motor.

Acknowledgements

This work was financially supported by the 111 Project (Grant No. D18019), Laboratory of Lingnan Modern Agriculture Project (Grant No. NT2021009), the Leading Talents of Guangdong Province Program (Grant No. 2016LJ06G689), the National Natural Science Foundation of China (Grant No. 32271985), the Natural Science Foundation of Guangdong Province (Grant No. 2022A1515011008; No. 2022A1515011535), and Liaoning Provincial Education Department Key Research Project (Grant No. LSNZD 202005).

[References]

- [1] Chen S D, Lan Y B, Zhou Z Y, Deng X L, Wang J. Research advances of the drift reducing technologies in application of agricultural aviation spraying. *Int J Agric & Biol Eng*, 2021; 14(5): 1–10.
- [2] Teske M E, Wachspress D A, Thistle H W. Prediction of aerial spray release from UAV. *Transactions of the ASABE*, 2018; 61(3): 909–918.
- [3] Wang J. Spray model of single rotor unmanned plant protection machine and its application in tropical crops. Doctoral dissertation. Guangzhou: South China Agricultural University, 2020; 168p. (in Chinese)
- [4] Wang J, Lan Y B, Yao W X, Chen P C, Wang G B, Chen S D. Aerial spraying application of multi-rotor unmanned aerial vehicle on areca trees. *Int J Precis Agric Aviat*, 2020; 3(4): 51–64.
- [5] Zhang K P, Chen J G, Wang C Y, Han L B, Shang Z Z, Wang G B, et al. Evaluation of herbicides aerially applied from a small unmanned aerial vehicle over wheat field. *Int J Precis Agric Aviat*, 2020; 3(1): 49–53.
- [6] Zhang H Y, Lan Y B, Wen S, Xu T Y, Yu F H. Research progress in rotor airflow model of plant protection UAV and droplet motion mechanism. *Transaction of the CSAE*, 2020; 36(22): 1–12. (in Chinese)
- [7] Chen P C, Lan Y B, Douzals J-P, Ouyang F, Wang J, Xu W C. Droplet distribution of Unmanned Aerial Vehicle under several spray volumes and canopy heights in the cotton canopy. *Int J Precis Agric Aviat*, 2020; 3(4): 74–79.
- [8] Zhan Y L, Chen P C, Xu W C, Chen S D, Han Y F, Lan Y B, et al. Influence of the downwash airflow distribution characteristics of a plant protection UAV on spray deposit distribution. *Biosystems Engineering*, 2022; 216: 32–45.
- [9] Zhang H Y, Lan Y B, Wen S, Chen C L, Xu T Y, Chen S D. A modelling approach of spray retention on rice in plant protection using unmanned aviation vehicle. *Transaction of the CSAE*, 2022; 38(18): 40–50. (in Chinese)
- [10] Chen S D. Research on droplet deposition mechanism and operating parameters of plant protection UAV for Rice. PhD dissertation. Guangzhou: South China Agricultural University, 2018; 119p. (in Chinese)
- [11] Zhang H Y. Experiment study on the performance of the aerial electrostatic spray system applied in UAV. Master dissertation. Guangzhou: South China Agricultural University, 2018; 81p. (in Chinese)
- [12] Yoon S, Lee H C, Pulliam T H. Computational analysis of multi-rotor flows. In: 54th AIAA Aerospace Sciences Meeting, San Diego: SCI Tech Forum, 2016; Paper No. 0812. doi: 10.2514/6.2016-0812.
- [13] Hwang J Y, Jung M K, Kwon O J. Numerical study of aerodynamic performance of a multirotor unmanned-aerial-vehicle configuration. *Journal of Aircraft*, 2015; 52(3): 839–846.
- [14] Yang F B, Xue X Y, Cai C, Zhou Q Q. Effects of down wash airflow in hover on droplet motion law for multi-rotor unmanned plant protection machine. *Transactions of the CSAE*, 2018; 34(2): 64–73. (in Chinese)
- [15] Tang Q, Zhang R R, Chen L P, Xu G, Deng W, Ding C C, et al. High-accuracy, high-resolution downwash flow field measurements of an unmanned helicopter for precision agriculture. *Computers and Electronics in Agriculture*, 2020; 173: 105390.
- [16] Guo Q W, Zhu Y Z, Tang Y, Hou C J, He Y, Zhuang J J, et al. CFD simulation and experimental verification of the spatial and temporal distributions of the downwash airflow of a quad-rotor agricultural UAV in hover. *Computers and Electronics in Agriculture*, 2020; 172: 105343.
- [17] Li J Y, Lan Y B, Shi Y Y. Research progress on airflow characteristics and field pesticide application system of rotary-wing UAV. *Transactions of the CSAE*, 2018; 34(12): 104–118. (in Chinese)
- [18] Liu X. Research on distribution regularity of downwash airflow velocity in rotor flow field of single rotor plant protection UAV. PhD dissertation. Daqing: Heilongjiang Bayi Agricultural University, 2019; 136p. (in Chinese)
- [19] Tang Q, Zhang R R, Chen L P, Deng W, Xu M, Xu G, et al. Numerical simulation of the downwash flow field and droplet movement from an unmanned helicopter for crop spraying. *Computers and Electronics in Agriculture*, 2020; 174: 105468.
- [20] Zhang H Y, Lan Y B, Shen N W, Wu J Y, Wang T, Han J, et al. Numerical analysis of downwash flow field from quad-rotor unmanned aerial vehicles. *Int J Precis Agric Aviat*, 2020; 3(4): 1–7.
- [21] Wen S, Han J, Ning Z H, Lan Y B, Yin X C, Zhang J T, et al. Numerical analysis and validation of spray distributions disturbed by quad-rotor drone wake at different flight speeds. *Computers and Electronics in Agriculture*, 2019; 166: 105036.
- [22] Wen S, Han J, Lan Y B, Yin X C, Lu Y H. Influence of wing tip vortex on drift of single rotor plant protection unmanned aerial vehicle. *Transactions of the CSAM*, 2018; 49(8): 127–137. (in Chinese)
- [23] Khan I, Aidun C K. Direct numerical simulation of saturated deformable porous media using parallel hybrid Lattice-Boltzmann and finite element method. *International Journal for Numerical Methods in Engineering*, 2010; 86(12): 1379–1395.
- [24] Xiong Q, Khosravi A, Nabipour N, Doranehgard M H, Sbaghmoghadam A, Ross D. Nanofluid flow and heat transfer due to natural convection in a semi-circle/ellipse annulus using modified lattice Boltzmann method. *International Journal of Numerical Methods for Heat & Fluid Flow*, 2019; 29(12): 4746–4763.
- [25] Nabavizadeh S A, Barua H, Eshraghi M, Felicelli S D. A multiple-grid lattice Boltzmann method for natural convection under low and high Prandtl numbers. *Fluids*, 2021; 6(4): 148.
- [26] Krüger T, Kusumaatmaja H, Kuzmin A, Shardt O, Silva G, Viggen E M. The lattice Boltzmann method: Principles and Practice. Springer Cham, 2017; 694p.
- [27] Wang L, Xu M, Hou Q H, Wang Z W, Lan Y B, Wang S M. Numerical verification on influence of multi-feature parameters to the downwash airflow field and operation effect of a six-rotor agricultural UAV in flight. *Computers and Electronics in Agriculture*, 2021; 190: 106452.
- [28] Cui X W, Yao X L, Wang Z K, Liu M H. A coupled Volume Penalization-Thermal Lattice Boltzmann method for thermal flows. *International Journal of Heat and Mass Transfer*, 2018; 127(Part A): 253–266.
- [29] Zhang H, Qi L J, Wu Y L, Musiu E M, Cheng Z Z, Wang P. Numerical simulation of airflow field from a six-rotor plant protection drone using lattice Boltzmann method. *Biosystems Engineering*, 2020; 197: 336–351.